Iterative time reversal in the ocean

H. C. Song, W. A. Kuperman, and W. S. Hodgkiss
Marine Physical Laboratory, Scripps Institution of Oceanography, University of California, San Diego, La Jolla, California 92093-0701

T. Akal and C. Ferla
SACLANT Undersea Research Center, 19138 La Spezia, Italy

(Received 8 May 1998; accepted for publication 22 February 1999)

The iterative time-reversal process focusing on the strongest scatterer in a multitarget medium has been described theoretically in terms of eigenvalues and eigenvectors of a time-reversal operator $\mathbf{K}^*\mathbf{K}$ in ultrasonics [Prada *et al.*, J. Acoust. Soc. Am. **97**, 62–71 (1995)]. In this paper, we extend the concept of iterative time-reversal to waveguide propagation in the ocean. For a single target, the iterative time-reversal process results in a minor improvement in spatial focusing. However, data from a recent experiment in the Mediterranean Sea [Kuperman *et al.*, J. Acoust. Soc. Am. **103**, 25–40 (1998)] illustrates the importance of the waveguide and source transducer characteristics even in the single target case. When the ocean contains several reflectors, iterative time-reversal focuses on the target corresponding to the largest eigenvalue of the time-reversal operator, which depends not only on the reflectivity of the targets, but also on the complex propagation effects between the targets and time-reversal mirror. Analysis of the experimental data for a single target and simulation results with multiple targets in the ocean are presented. © *1999 Acoustical Society of America.* [S0001-4966(99)02306-1]

PACS numbers: 43.30.Yj, 43.30.Vh, 43.30.Wi, 43.30.Re [DLB]

INTRODUCTION

Over the past several years, acoustic time-reversal mirrors (TRM) have been studied extensively in medical ultrasound,[1–3] nondestructive testing,[4,5] and ocean acoustics.[6–7] A good overview of TRM is provided in the recent paper by Fink.[8] Unlike an ordinary mirror that produces the virtual image of an acoustic object, the TRM produces a real acoustic image of the probe source (PS) by converting a divergent wave emitted from the acoustic PS into a convergent wave focusing on the PS. A TRM can be realized by a source-receive array. The incident signal is received, time reversed, and retransmitted from an array of sources collocated with the receivers.

When the medium contains several reflectors, the time-reversal process can be iterated in order to focus on the most reflective one, as demonstrated in ultrasonic laboratory acoustic experiments.[9–11] The theory of the iterative time-reversal mirror has been presented by Prada *et al.*[11] in terms of eigenvalues and eigenvectors of the time-reversal operator $\mathbf{K}^*(f)\mathbf{K}(f)$, where f is frequency,* denotes complex conjugation, and $\mathbf{K}(f)$ is the transfer matrix of the array transducers ensonifying a time-invariant scattering medium. Prada *et al.* further extended the iterative time-reversal process to focus on a specific target by decomposition of the time-reversal operator called the DORT method.[12]

Iterative time reversal in the ocean has been demonstrated recently in an experiment conducted in the Mediterranean Sea.[7] In this paper, we revisit the experimental results for a single target and investigate further iterative time reversal in the ocean for multiple targets. In our analysis, boundary reverberation is not considered explicitly since we assume the waveguide boundaries are smooth.

In Sec. I, we review the theory of the iterative time-reversal mirror developed in free-space ultrasonics. Section II describes the experimental results with a single target in the ocean. Section III presents simulation results in the ocean with two targets. Finally, conclusions are given in Sec. IV.

I. ITERATIVE TIME REVERSAL

The theory of iterative time reversal has already been presented in Ref. 11. We review briefly the basics of iterative time reversal assuming pointlike targets and single scattering, and then derive the intensity of the sound field over the iterations. The pointlike scatterers are small compared to the wavelength and have a spherical response to the incident pressure field.

A. Overview of theory

Assume that the array of transducers for the TRM consists of M similar elements and that the medium contains d pointlike scatterers with reflection coefficients $C_1(f)$, $C_2(f),\ldots,C_d(f)$. In order to express the received signals as a function of those transmitted, we define for each pair of transducers an interelement impulse response $k_{lm}(t)$, from element l to element m (Fig. 1). This impulse response includes all of the propagation effects through the medium under investigation as well as the acousto-electrical responses of the two elements. Let $a_t(t)$ and $a_r(t)$ be the transducers' acousto-electrical response in transmission and in reception with Fourier transforms $A_t(f)$ and $A_r(f)$, respectively. For each frequency component f, a transfer matrix is defined as $\mathbf{K}(f)=(K_{lm}(f))_{1\leq l,m\leq M}$, where $K_{lm}(f)$ is a Fourier transform of $k_{lm}(t)$.

Assuming pointlike targets and single scattering,[11] the transfer matrix $\mathbf{K}$ can then be written as

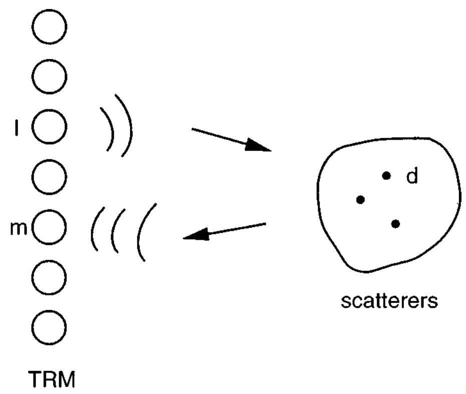

FIG. 1. Interelement impulse response k_{lm}.

$$\mathbf{K}(f)=A_t(f)A_r(f)\sum_{i=1}^{d} C_i(f)\mathbf{H}_i(f)\mathbf{H}_i^T(f), \tag{1}$$

where $\mathbf{H}_i=[H_{i1},H_{i2},\ldots,H_{iM}]^T$ is a column vector of transfer functions between the ith scatterer and M elements of the TRM, and T denotes a transpose operation. Note that $\mathbf{K}(f)$ is symmetrical due to reciprocity. For convenience, we drop the frequency dependence f and suppress the acousto-electrical responses A_t and A_r in most of the following analysis, since they can be absorbed into each of the transfer function $\mathbf{H}_i$ as a scale factor, except in instances where the transducer characteristics must be considered.

Once we measure a transfer matrix $\mathbf{K}$, an iterative TRM can be described theoretically in terms of eigenvalues and eigenvectors of a Hermitian matrix $\mathbf{K}^*\mathbf{K}$ referred to as a time-reversal operator in Refs. 10–12. Here, we confine our interests to the case of ideal separation of the reflectors[11] by assuming the orthogonality of transfer functions

$$\mathbf{H}_i^T\mathbf{H}_j^*=0 \quad \text{for } i\neq j. \tag{2}$$

This assumption is valid, for example, for reflectors at the same range but different depths in an ideal waveguide due to the ''closure'' or completeness property of the orthonormal modal functions if the source–receive array (SRA) spans most of the water column and adequately samples most of the modes so that the orthogonality condition is satisfied.[7] In practice, however, there are only a finite number of propagating modes in an oceanic waveguide so that Eq. (2) is satisfied only approximately, resulting in depth resolution of D/N where D is the water depth and N is the number of propagating modes.[13]

In case of ideal separations, the Hermitian operator can be decomposed into

$$\mathbf{K}^*\mathbf{K}=\sum_{i=1}^{d} |C_i|^2|\mathbf{H}_i|^4 \frac{\mathbf{H}_i^*\mathbf{H}_i^T}{|\mathbf{H}_i|^2}, \tag{3}$$

where the eigenvectors are $\mathbf{H}_i^*$ and the corresponding eigenvalues λ_i including the acousto-electrical responses are

$$\lambda_i=|A_tA_r|^2|C_i|^2|\mathbf{H}_i|^4. \tag{4}$$

Note that each eigenvector of the operator $\mathbf{H}_i^*$ is associated with one of the pointlike scatterers, exactly the vector signal after time reversal for one scatterer considered separately. The eigenvalues are positive because the operator $\mathbf{K}^*\mathbf{K}$ is Hermitian. The eigenvalues depend both on the reflectivity C_i and on the propagation effects $|\mathbf{H}_i|$ which could be more significant in a complex oceanic waveguide due to the 4th power as compared to the 2nd power in C_i as revealed in the following sections. The impact of the acousto-electrical responses of the transducers on the iterative time-reversal mirror also will be addressed in Sec. II.

B. Intensity at the *n*th iteration

In this section, we derive the intensity of the field in terms of eigenvalues of the time-reversal operator $\mathbf{K}^*\mathbf{K}$ for ideally resolved scatterers. It is shown in Ref. 11 that the pressure field resulting from an iterative process converges differently toward odd and even limits. In ultrasonics, the effect of focusing has been displayed in the vicinity of targets by the maximum magnitude of the pressure field. The probe pulse for ultrasonic laboratory experiments typically is a half cycle of the carrier frequency around 3.5 MHz.[8] However, in our ocean acoustic experiment where a 22-cycle pure-tone pulse with carrier frequency of 445 Hz was used,[7] we can better represent the focusing effect in terms of energy over a segment of data rather than the pressure itself.

Let $\mathbf{P}[0]$ be the complex pressure vector received by each scatterer position after initial ensonification of the field by an input vector on the TRM, $\mathbf{E}[0]$, such that $\mathbf{P}[0]=A_t\mathbf{H}^T\mathbf{E}[0]$ where $\mathbf{H}=[\mathbf{H}_1,\mathbf{H}_2,\ldots,\mathbf{H}_d]$ is an $M\times d$ transfer function matrix. The pressure field of the scatterers at the iteration number n, $\mathbf{P}[n]$, can then be related to the pressure field at the iteration number $n-1$, $\mathbf{P}[n-1]$, as follows (see Fig. 1 in Ref. 12):

$$\mathbf{P}[n]=\mathbf{H}^T(\mathbf{HCP}[n-1])^*=\mathbf{H}^T\mathbf{H}^*\mathbf{C}^*\mathbf{P}^*[n-1], \tag{5}$$

where $\mathbf{C}=\mathrm{diag}(C_1,C_2,\ldots,C_d)$ is a diagonal matrix due to the single scattering assumption. Since the columns of $\mathbf{H}$ are orthogonal to each other for ideal separations of the reflectors as shown in Eq. (2), the intensity of the field by ith scatterer at iteration number n simply reduces to

$$I_i[n]=|C_i|^2|\mathbf{H}_i|^4I_i[n-1]=\lambda_iI_i[n-1]=\lambda_i^nI_i[0], \tag{6}$$

where $I_i[0]=|P_i[0]|^2$. For broadband pulse propagation in a time-reversal mirror, a total energy can be obtained using Parsevel's relation over the frequency band of the signal,

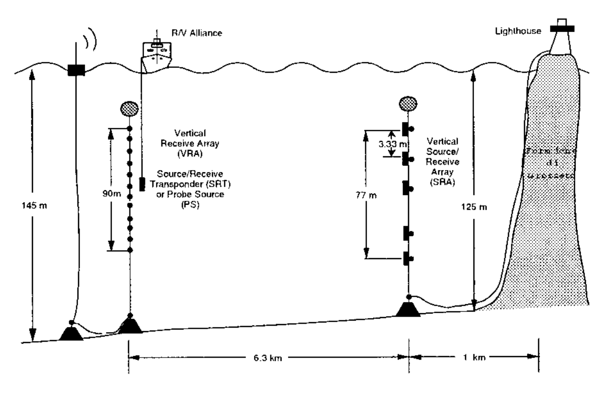

FIG. 2. Experimental setup of April 1996 phase conjugation experiment.

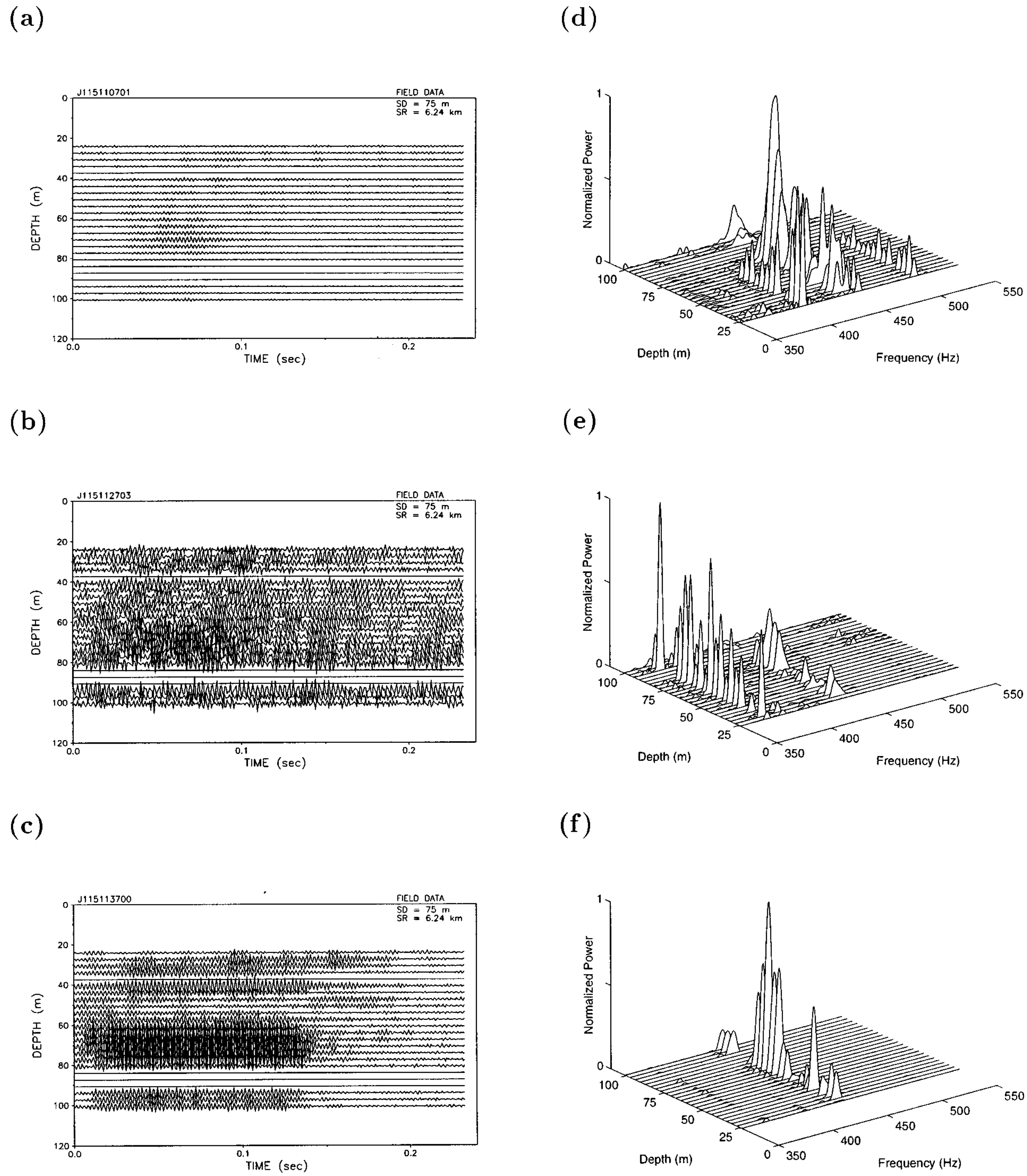

FIG. 3. Experimental results from iterative time reversal received on the SRA for a simulated scatterer (SRT) located at 75 m depth and 6.24 km range from the SRA. (a)–(c) display the pulse data received on the SRA at iterations #1, #11, and #16, respectively. (d)–(f) are the corresponding normalized spectra. Note that four elements of the SRA were dead during the experiment. Typically, there are three spectral-noise components around 410, 460, and 510 Hz, as shown in (d). The dominant noise component around 370 Hz in (e) is due to a small freighter passing 1 km away from the SRA.

$$E_i[n]=\int \lambda_i^n(f)I_i[0](f)df. \tag{7}$$

II. ITERATIVE PHASE CONJUGATION IN THE OCEAN

Phase conjugation as applied to underwater acoustics has been explored theoretically[6] and demonstrated experimentally in the ocean.[7] Here, we describe the implementation of iterative phase conjugation using the geometry of the TRM experiment shown schematically in Fig. 2 and then analyze the experimental results. More details on the theory and experiment are given in Ref. 7.

A. Experimental setup: Acoustic Ping-Pong

The April 1996 TRM experiment utilized a vertical source–receive array (SRA) spanning 77 m of a 125-m water column with 20 sources and receivers and a single source/receive transponder (SRT) (echo repeater) or probe source

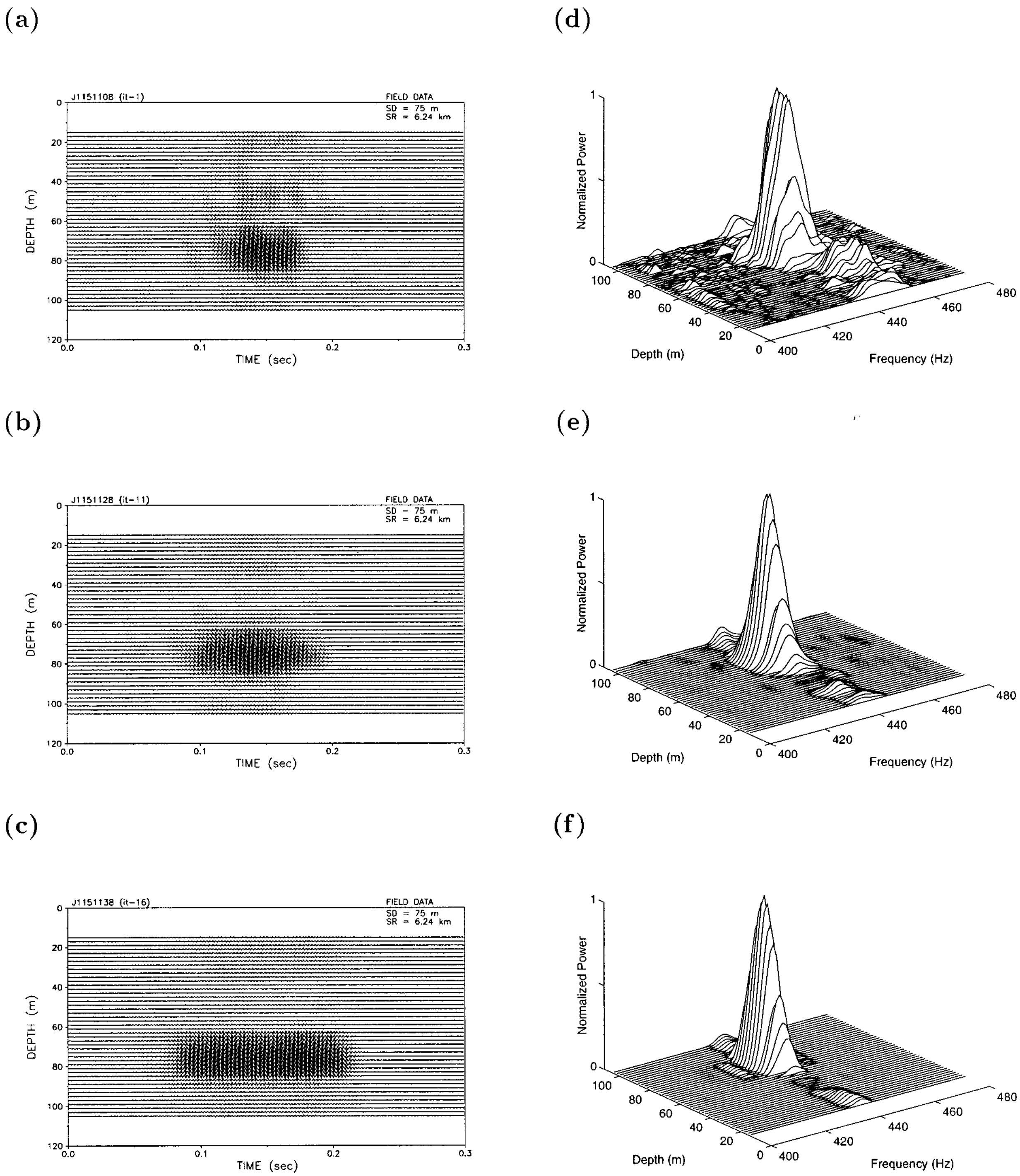

FIG. 4. Experimental results from iterative time reversal received on the VRA for a simulated scatterer (SRT) located at 75 m depth and 6.24 km range from the SRA. (a)–(c) display the pulse data received on the VRA from the time-reversed transmissions of the pulses shown in Fig. 3(a)–(c) at iterations #1, #11, and #16, respectively. (d)–(f) are the corresponding normalized spectra.

(PS) collocated in range with another vertical array (VRA) of 46 elements spanning 90 m of a 145-m water column located 6.3 km away from the SRA. Phase conjugation was implemented by transmitting a 50-ms pulse with center frequency of 445 Hz from the PS to the SRA, digitizing the received signal, and retransmitting the time-reversed signal from all sources of the SRA. The transmitted signal was then received at the VRA. An assortment of runs was made to examine the structure of the focal point region and the temporal stability of the process. These results are reported in Ref. 7.

For the iterative phase conjugation experiment, the probe source with collocated receiver (an element of the VRA) now acts as a simulated scatterer (SRT). The iterative time-reversal process is initiated by transmitting a 50-ms pulse with equal amplitudes on all elements from the SRA to ensonify the waveguide. The transmission is captured at 75 m depth by the SRT and retransmitted (echoed) back to the SRA. The SRA time reverses the received signal and retransmits it from all the SRA sources back to the VRA. This acoustic Ping-Pong process was repeated many times over an

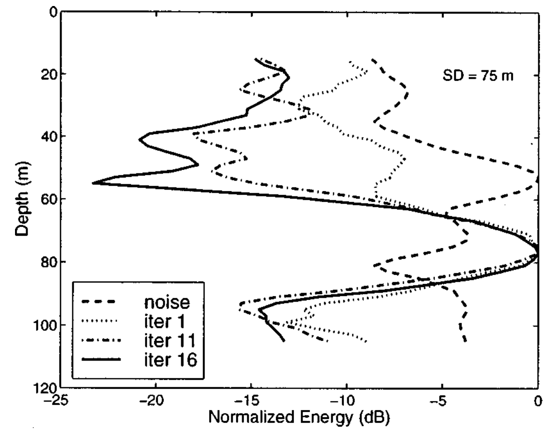

FIG. 5. Acoustic Ping-Pong results between the SRA and a transponder at 75 m depth and 6.24 km range. Displayed is the energy over a 0.3-s window on the VRA as a function of depth for iterations #1, #11, and #16. The dashed line indicates the energy of the simulated backpropagation of the noise shown in Fig. 8(b).

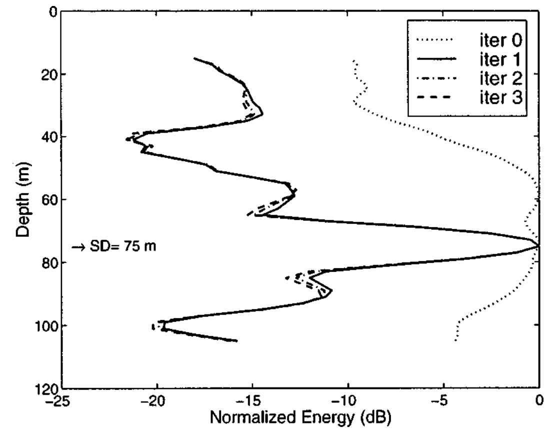

FIG. 6. Simulation results for a single target at 75 m depth. The energy over a 0.3-s window as a function of depth on the VRA for iterations #1 to #3 shows no significant improvement in focusing over the iteration process. The dotted line indicates the ensonified field resulting from transmitting a 50-ms pulse with equal amplitudes on all elements of the SRA. Note that the field decreases more rapidly towards the surface compared to the bottom, due to the downward-refracting sound-speed profile employed in the model.

hour with 2 min between each round trip. Here, we report on the experimental data obtained on JD 115 (24 April 1996) from 11:06 to 11:38 Z for a total of 17 successive iterations.

B. Experimental results

Figure 3 shows the pulse data and corresponding spectra received on the SRA for iterations #1, #11, and #16. The simulated scatterer (SRT) was located at 75 m depth and 6.24 km range. Here, we refer to iteration #1 as the first time-reversal operation after initial ensonification. The data are a combination of signal and noise. A 233-ms segment of data was digitized and time reversed for retransmission to the VRA at each iteration. Note in the time-series displays that the signal level increases over the iterations due to an iterative loop gain being greater than 1. Also note in Fig. 3(b) that the signal is hardly visible due to shipping noise around 370 Hz. Typically, there are three spectral-noise components around 410, 460, and 510 Hz, as shown in Fig. 3(d). As will be seen, these noise components turn out to be an important factor in the analysis of the experimental data.

Figure 4 shows the time-series data and corresponding spectra as received on the VRA from the time-reversed transmission of the pulses shown in Fig. 3. The time series are normalized with respect to the maximum amplitude as opposed to Fig. 3, where no normalization has been applied. Two observations can be made. At the first iteration shown in Fig. 4(a), we clearly see a vertical spatial focusing of ± 15 m around the 75-m SRT depth as well as a temporal compression to 50 ms (the original pulse length) *plus* the time spread of the sound channel due to the initial ensonification by the SRA which is not significant, as will be seen in Fig. 11(a). Note, however, that the time series duration expands significantly over the sequence of iterations. Expansion of the signal duration is confirmed by the more narrow bandwidth of the corresponding spectra over the sequence of iterations on the right side of Fig. 4. Second, Fig. 4(b) shows very good spatial focusing in the presence of the dominant shipping noise around 370 Hz, as shown in Fig. 3(b).

An alternative way to display the VRA data is to plot the energy over a 0.3-s window as a function of depth and iteration. Due to the sidelobe suppression between 40–60 m above the SRT depth of 75 m, Fig. 5 appears to indicate an increase in focusing over the sequence of iterations. However, the iterative simulation results for a single target in Fig. 6 suggest only a minor improvement in spatial focusing. The environmental model used for the simulations throughout this paper is displayed in Fig. 7. Note that Fig. 6 also indicates the degree to which orthogonality of the transfer functions as described in Eq. (2) is satisfied.

The apparent improvement in spatial focusing is due to the noise components observed on the SRA (especially around 460 Hz, close to the carrier frequency of 445 Hz). As mentioned earlier, typically there are three noise components around 410, 460, and 510 Hz embedded in the observed data on the SRA. A typical noise-alone time series observed on the SRA is shown in Fig. 8(b), along with its corresponding normalized spectrum in Fig. 8(d). The result of backpropagating the noise-alone time series to the VRA in simulation

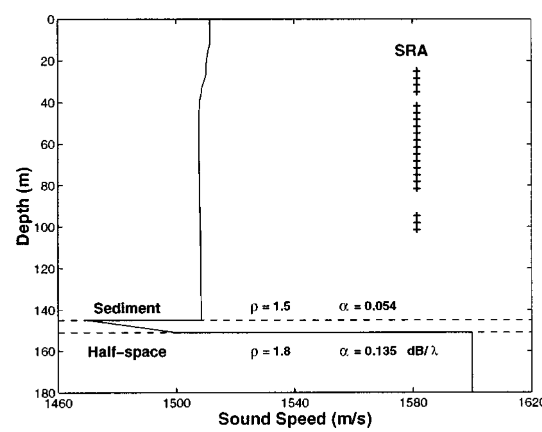

FIG. 7. Sound-speed profile used in the simulations along with the bottom geoacoustic parameters. The depths of the SRA elements are also indicated.

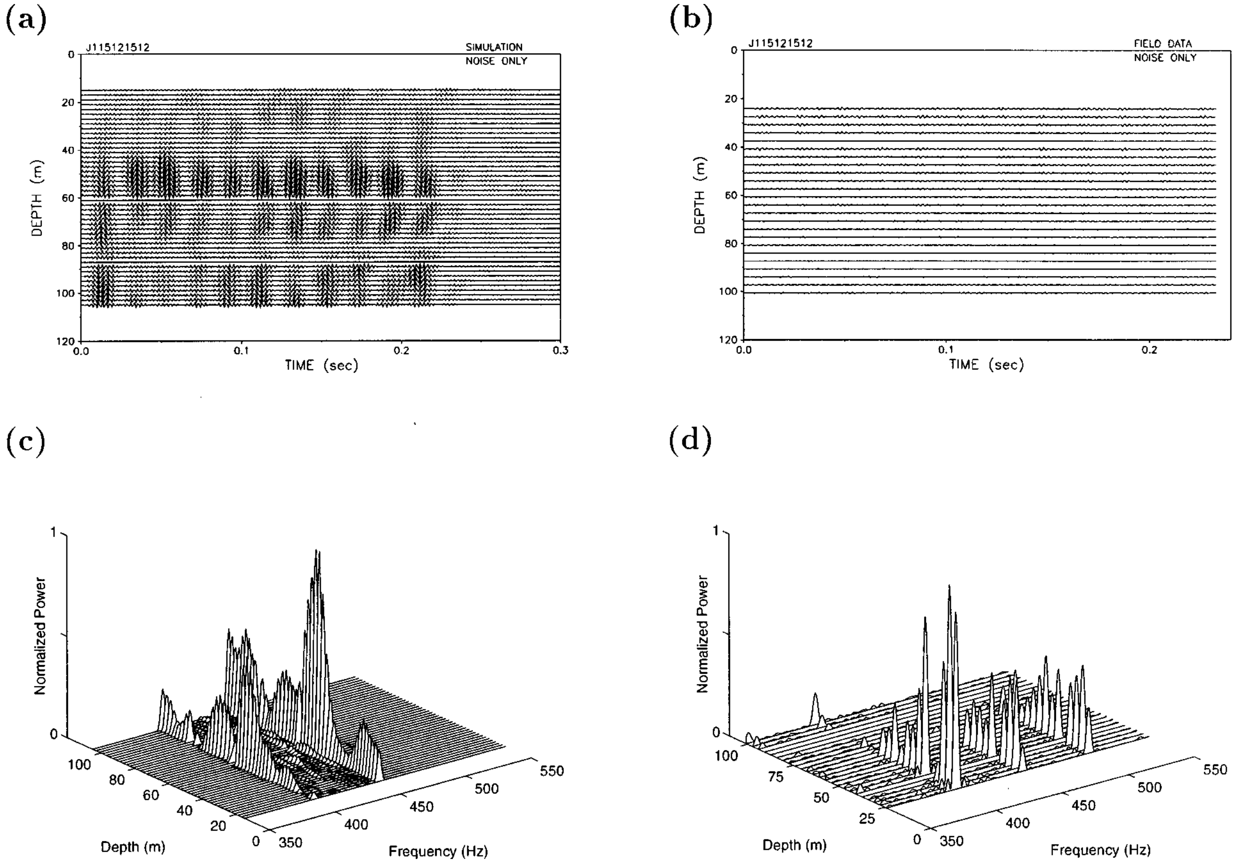

FIG. 8. Simulated backpropagation (a) and corresponding spectrum (c) using noise-alone data observed on the SRA shown in (b). The three noise components are shown in (d) around 410, 460, and 510 Hz. Note that the spectral content in (c) extends only up to 480 Hz because the higher-frequency component is attenuated substantially by the SRA transducer characteristics.

and the corresponding spectrum are displayed in Fig. 8(a) and (c), respectively.

Note that the backpropagated noise contributes substantially to the field between 40 and 60 m depth, as is also shown by the dashed line in Fig. 5. At the beginning of the iteration process, this backpropagated noise field degrades the apparent spatial focusing significantly, as shown in Fig. 5. Over the sequence of iterations, however, the noise level becomes negligible compared to the signal level. The signal level increases due to the iterative loop gain being greater than 1 (see Fig. 3). Thus, after a number of iterations we attain a spatial focusing that would be similar to the spatial focusing without noise, as shown in Fig. 6.

Aside from the noise issues, Fig. 9 shows the normalized spectra (dB) at the target depth of 75 m for iterations #1, #11, and #16 selected from (d)–(f) in Fig. 4. It is interesting to note a 5-Hz shift in the center frequency from 445 to 440 Hz over the sequence of iterations as well as the more narrow bandwidth described earlier.

As derived in Sec. I B, the intensity of the sound field at a single target after the nth iteration is $I_1[n]=\lambda^n(f)I_1[0]$, with the initial ensonification of $I_1[0]=|A_t|^2|\mathbf{H}_1^T\mathbf{E}[0]|^2$. The initial input vector $\mathbf{E}[0]$ is equal to $S(f)\mathbf{I}$, where $S(f)$ is the source spectrum of the pulse initially transmitted from the SRA and $\mathbf{I}$ is a unit vector. The expression for the eigenvalue of the time-reversal operator λ is given by Eq. (4), which depends upon the SRA source transducer functions $A_t(f)$ and $A_r(f)$, the medium propagation characteristics $\mathbf{H}_1(f)$, and the target reflectivity C_1. In the experimental data, the SRT (echo repeater) transducer was identical to those used in the source array (SRA). Accordingly, C_1 in Eq. (4) needs to be multiplied by an additional factor of $A_t(f)$. On the other hand, the receiver hydrophones of the SRA have an almost flat frequency response over the frequency band involved [i.e., $A_r(f)=\text{const}$].

Figure 10 compares the characteristics of the three functions involved: $|\mathbf{H}(f)|$, $|A_t(f)|$, and $I[0]$. Note the fourth

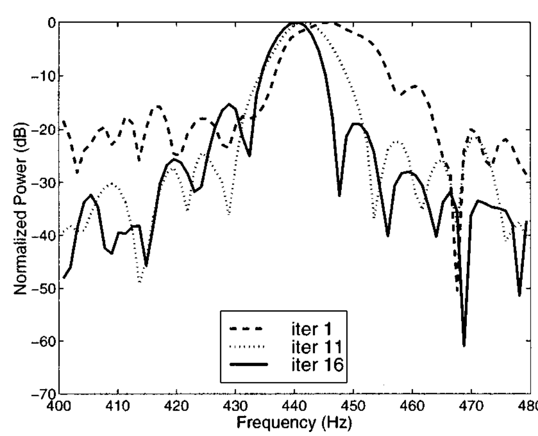

FIG. 9. Normalized spectra (dB) at the target depth of 75 m for iterations #1, #11, and #16 from (d)–(f) in Fig. 4. Note the more narrow bandwidth and shift in the center frequency from 445 to 440 Hz over the sequence of iterations.

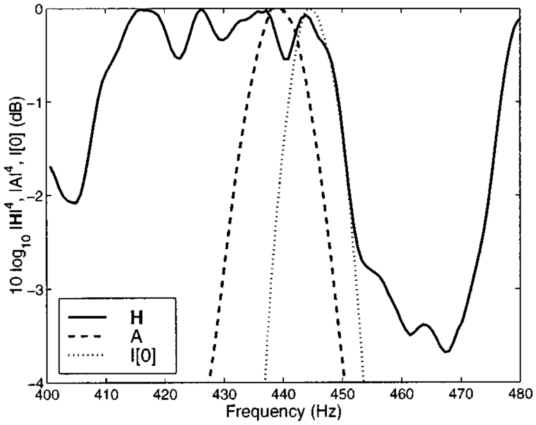

FIG. 10. The medium propagation characteristics $|\mathbf{H}(f)|$ (solid) between the target at 75 m depth and the SRA, the source transducer characteristics $|A_t(f)|$ (dashed), and the initial ensonification at the 75-m target depth $I[0](f)$ (dotted) determined mainly by the source signal spectrum $|S(f)|$.

power of $|\mathbf{H}(f)|$ and $|A_t(f)|$ as compared to the initial ensonification $I[0]$ to emphasize their contribution at each iteration. As shown by the dotted line, $I[0]$ looks similar to the source spectrum $|S(f)|$, whose center frequency is 445 Hz. The dashed line displays a source transducer function $|A_t(f)|$, which has a resonance at approximately 440 Hz and a 3-dB bandwidth of approximately 40 Hz. The magnitude of the complex transfer function vector $|\mathbf{H}(f)|$ shows a band-pass characteristic with a cutoff beyond 450 Hz. Multiplying these transfer functions at the SRA and SRT repetitively over the sequence of iterations results in a narrower bandwidth of the signal as well as a-5-Hz shift in the center frequency. This frequency shift should be distinguished from a Doppler shift due to either source or receiver motion.

III. MULTIPLE TARGETS IN THE OCEAN

In this section, we investigate the case of multiple targets in the ocean through simulations. For simplicity, we consider two pointlike targets at the same range (6.3 km), but different depths of 40 and 75 m, denoted by T1 and T2, respectively. Without loss of generality, we assume a flat frequency response of the transducers. Noise is not included in this simulation.

First, consider two targets with equal strength, i.e., $C_1 = C_2$. As in the single-target case, we ensonify the acoustic waveguide by transmitting 50-ms pure-tone pulse with equal amplitude from all sources of the SRA to the VRA. Figure 11(a) shows the initial ensonified field $I[0]$ at the VRA, which is not homogeneous with depth as opposed to the free-field case. As noted earlier, pulse spreading is not significant mainly due to the narrow bandwidth of the pulse employed. Note also that we have much weaker energy near the surface due to the downward-refracting sound-speed profile included in the environmental model.

Figure 11(b) and (c) show results after the first and third iterations, respectively. Note that target T1 at the shallower depth is barely visible after the first iteration and disappears almost completely after the third iteration. This observation can be explained from Eqs. (6) and (7). In our example, the ratio of the ensonified field $I_1[0]/I_2[0] \cong 0.24$ and the ratio

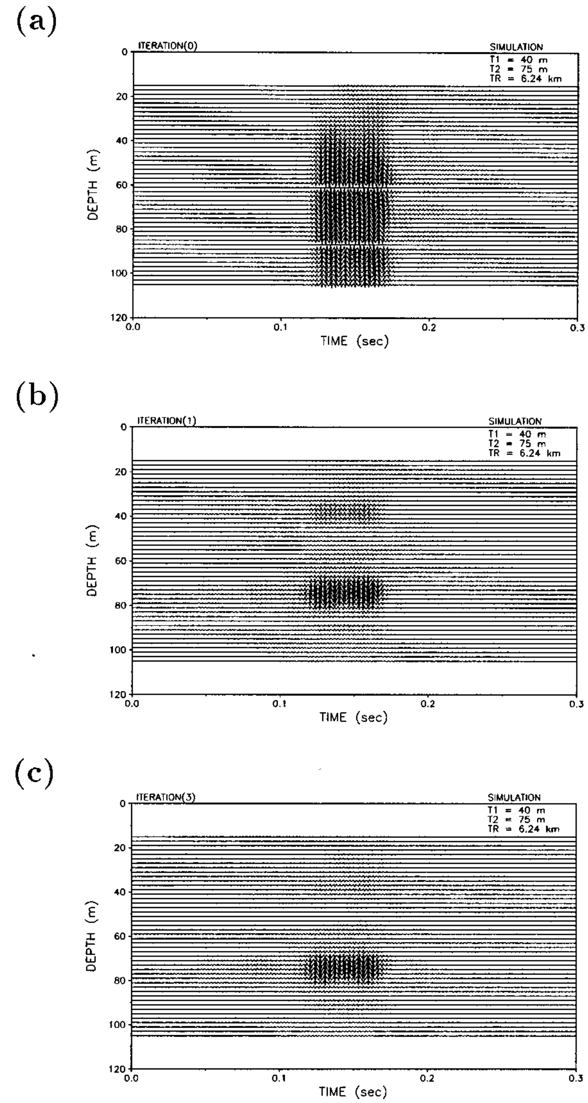

FIG. 11. Simulation results for two pointlike targets with equal reflectivities at depths of 40 and 75 m. (a) Ensonified field on the VRA by transmitting a 50-ms pulse with equal amplitudes from all sources of the SRA. (b) Results after the first iteration. (c) Results after the third iteration. Note that even after the first iteration, the target T1 at shallower depth is hardly visible.

of eigenvalues $\lambda_1/\lambda_2 = |\mathbf{H}_1|^4/|\mathbf{H}_2|^4 \cong 0.44$ at the center frequency of 445 Hz for targets with the same reflectivity. As shown in Fig. 12, after one iteration the intensity of T1 drops almost 7–8 dB with respect to the level of T2 when integrated over the frequency band.

This example demonstrates that an iterative time-reversal process in an underwater waveguide does not necessarily focus on the most reflective target. The ''effective'' reflectivity includes the propagation effects between the targets and the SRA. The target with the largest effective reflectivity is the one which corresponds to the largest eigenvalue of the time-reversal operator.

The next question then is, under what condition can we focus on the shallow target T1. Since the propagation effects are determined by the relative position of the targets with respect to the SRA, the target strength of T1 must be strong enough to compensate the smaller $|\mathbf{H}_1|$ as compared to $|\mathbf{H}_2|$ such that $\lambda_1/\lambda_2 > 1$. We already have computed that the ratio

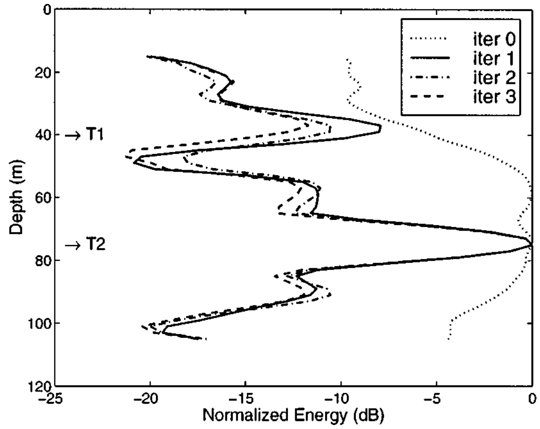

FIG. 12. Simulation results for two targets with equal reflectivities at depths of 40 and 75 m. The energy over a 0.3-s window as a function of depth on the VRA is plotted for iterations 0 to 3. The dotted line indicates the initial ensonified field.

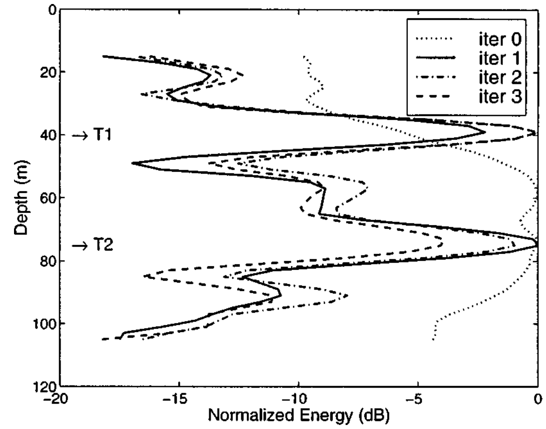

FIG. 14. Simulation results for two targets with unequal reflectivities at depths of 40 and 75 m. The energy over a 0.3-s window as a function of depth on the VRA is plotted for iterations 0 to 3. The dotted line indicates the initial ensonified field.

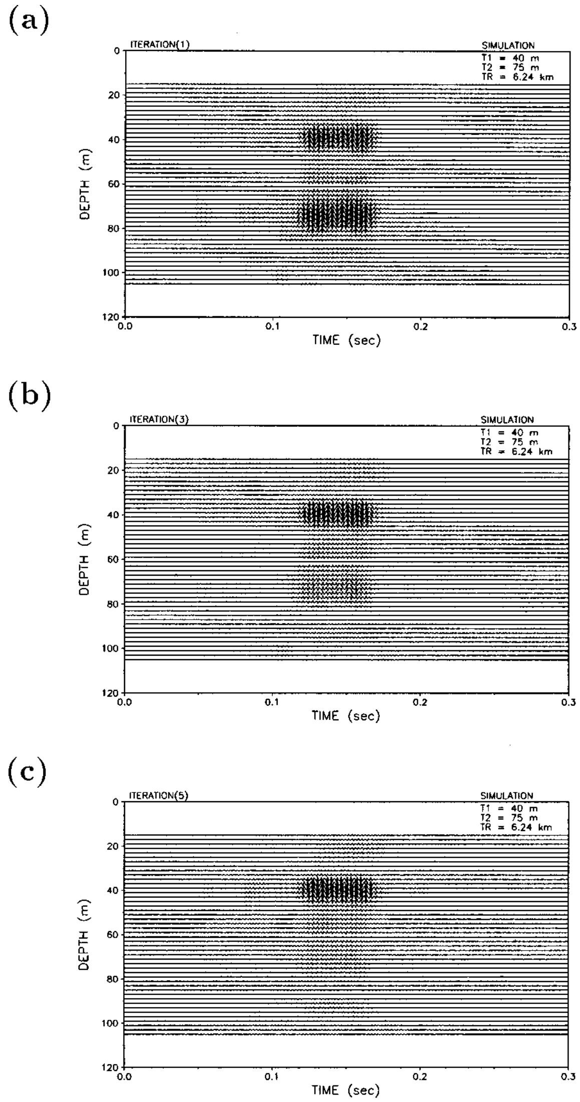

FIG. 13. Simulation results for two pointlike targets with unequal reflectivities at depths of 40 and 75 m. The ratio of reflectivities is $C_1/C_2=2$. (a), (b), and (c) are the results after iterations #1, #3, and #5, respectively. We see two targets after the first iteration. After five iterations, T1 dominates the field at the VRA.

of the eigenvalues is $\lambda_1/\lambda_2 \cong 0.44$ for the same reflectivities. Then, from Eq. (4) the target strength of T1 must be increased to greater than $1/\sqrt{0.44} \cong 1.5$. Figure 13 shows simulation results of iterative time reversal when the target strength at s.d.=40 m is twice that at s.d.=75 m, i.e., $C_1/C_2=2$. After the first iteration, the field strength at 75 m depth is still greater than that at 40 m, as shown in Fig. 14. However, successive iterations yields the stronger field at s.d.=40 m. By iteration 5, we clearly see that the field focuses at s.d.=40 m.

IV. CONCLUSIONS

The concept of an iterative time-reversal mirror has been extended to waveguide propagation in the ocean. For a single target, the iterative time-reversal process results in a minor improvement in spatial focusing. However, analysis of data from a recent experiment in the Mediterranean Sea did illustrate the importance of the waveguide and source transducer characteristics even in the single transducer case. Their combined effects through repeated multiplication over the iteration process resulted in narrowing of the pulse bandwidth along with a-5-Hz shift in the center frequency.

When we have multiple targets in free space, iterative time reversal selects out the most reflective target which corresponds to the largest eigenvalue of the time-reversal operator. In the waveguide case with smooth boundaries, the eigenvalues of the time-reversal operator are a function of the target reflectivities as well as the complex propagation characteristics of the medium. As shown in Eq. (4), the propagation characteristics are very important in an oceanic waveguide. Simulations with two targets at the same range but different depths were used to illustrate both of these effects on focusing.

ACKNOWLEDGMENTS

This research was supported by the Office of Naval Research Code 321US, Contract Nos. N00014-96-I-0065 and N00014-97-D-0003.

[1] O. Ikeda, ''An image reconstruction algorithm using phase conjugation for diffraction-limited imaging in an inhomogeneous medium,'' J. Acoust. Soc. Am. **85**, 1602–1606 (1989).
[2] M. Fink, ''Time-reversal mirrors,'' J. Phys. D **26**, 1330–1350 (1993).
[3] C. Dorme and M. Fink, ''Focusing in transmit–receive mode through inhomogeneous media: The time-reversal matched filter approach,'' J. Acoust. Soc. Am. **98**, 1155–1162 (1995).
[4] J. L. Thomas, P. Roux, and M. Fink, ''Inverse scattering analysis with an acoustic time-reversal mirror,'' Phys. Rev. Lett. **72**, 637–640 (1994).
[5] N. Chakroun, M. Fink, and F. Wu, ''Time reversal processing in ultrasonic nondestructive testing,'' IEEE Trans. Ultrason. Ferroelectr. Freq. Control **42**, 1087–1098 (1995).
[6] D. R. Jackson and D. R. Dowling, ''Phase conjugation in underwater acoustics,'' J. Acoust. Soc. Am. **89**, 171–181 (1991).
[7] W. A. Kuperman, W. S. Hodgkiss, H. C. Song, T. Akal, C. Ferla, and D. R. Jackson, ''Phase conjugation in the ocean: Experimental demonstration of an acoustic time reversal mirror,'' J. Acoust. Soc. Am. **103**, 25–40 (1998).
[8] Mathias Fink, ''Time-reversed acoustics,'' Phys. Today **50**, 34–40 (1997).
[9] C. Prada, F. Wu, and M. Fink, ''The iterative time reversal mirror: A solution to self-focusing in the pulse echo mode,'' J. Acoust. Soc. Am. **90**, 1119–1129 (1991).
[10] C. Prada and M. Fink, ''Eigenmodes of the time reversal operator: A solution to selective focusing in multiple-target media,'' Wave Motion **20**, 151–163 (1994).
[11] C. Prada, J. L. Thomas, and M. Fink, ''The iterative time reversal process: Analysis of the convergence,'' J. Acoust. Soc. Am. **97**, 62–71 (1995).
[12] C. Prada, S. Manneville, D. Spoliansky, and M. Fink, ''Decomposition of the time reversal operator: Detection and selective focusing on two scatterers,'' J. Acoust. Soc. Am. **99**, 2067–2076 (1996).
[13] E. C. Shang, ''Source depth estimation in waveguides,'' J. Acoust. Soc. Am. **77**, 1413–1418 (1985).